Submitted to ApJ 10/24/2014
Preprint typeset using LaTeX style emulateapj v. 11/10/09

arXiv:1410.6759v1 [astro-ph.SR] 24 Oct 2014

LATE-TIME NEAR-INFRARED OBSERVATIONS OF SN 2005DF

Tiara R. Diamond [1], Peter Hoeflich [1], and Christopher L. Gerardy[1,2]
[1]Department of Physics, Florida State University and
[2]Department of Physics, University of North Carolina, Charlotte
Submitted to ApJ 10/24/2014

ABSTRACT

We present late-time ($200 - 400$ day) near-infrared spectral evolution for the Type Ia supernova SN 2005df. The spectra show numerous strong emission features of [Co II], [Co III] and [Fe II] throughout the $0.8 - 1.8\,\mu$m region. As the spectrum ages, the cobalt features fade as would be expected from the decay of ^{56}Co to ^{56}Fe. We show that the strong and isolated [Fe II] emission line at $1.644\,\mu$m provides a unique tool to analyze near-infrared spectra of Type Ia supernovae. Normalization of spectra to this line allows separation of features produced by stable versus unstable isotopes of iron group elements. We develop a new method of determining the initial central density, ρ_c, and the magnetic field, B, of the white dwarf using the width of the $1.644\,\mu$m line. The line width is sensitive because of electron capture in the early stages of burning, which increases as a function of density. The sensitivity of the line width to B increase with time and the effects of the magnetic field shift towards later times with decreasing ρ_c. The initial central density for SN 2005df is measured as $\rho_c = 0.9(\pm0.2)$ (in $10^9\,\mathrm{g\,cm^{-3}}$), which corresponds to a white dwarf close to the Chandrasekhar mass ($\mathrm{M_{Ch}}$) with $\mathrm{M_{WD}} = 1.313(\pm0.034)\,\mathrm{M_\odot}$ and systematic error less than $0.04\,\mathrm{M_\odot}$. Within $\mathrm{M_{Ch}}$ explosions, however, the central density found for SN 2005df is very low for a H-accretor, possibly suggesting a helium star companion or a tidally-disrupted white dwarf companion. As an alternative, we suggest mixing of the central region. We find some support for high initial magnetic fields of strength 10^6 G for SN 2005df, however, 0 G cannot be ruled out because of noise in the spectra combined with low ρ_c.

Subject headings: line: identification – magnetic fields – supernovae: individual (SN 2005df)

1. INTRODUCTION

Type Ia supernovae (SNe Ia) are extremely important in astronomy because of their use in measuring cosmological distances and the opportunities they provide to study the physics of flames, instabilities, radiation transport, non-equilibrium systems, and nuclear and high energy physics. SNe Ia are bright time-dependent events which have been seen out to redshifts of $z = 1.71$ (Rubin et al. 2013). Although there is some variety in the absolute luminosity of these events, they have been shown to be standardizable by using characteristics of their light curves (Phillips 1993). With increasing numbers of SNe Ia being discovered, differences in spectra can be examined in order to create additional corrections to the standardization of these objects and to further hone our understanding of the progenitor systems, the cause of the explosion, and the propagation of material and energy due to the explosion. For overviews see Branch et al. (1995), Nomoto et al. (2003), Di Stefano et al. (2011), Di Stefano & Kilic (2012), Wang & Han (2012), and Hoeflich et al. (2013).

The consensus is that SNe Ia come from close binary systems and result from a degenerate carbon/oxygen (CO) white dwarf (WD) undergoing a thermonuclear runaway (Hoyle & Fowler 1960). There are multiple potential progenitor systems in addition to multiple explosion scenarios. In the double degenerate (DD) system, the binary system consists of two or more WDs. In the single degenerate (SD) system, the binary system may consist of a single WD and either a main sequence, helium star, or giant star companion (Nomoto et al. 1984; Hernanz et al. 1988; Piersanti et al. 2003; Lorén-Aguilar et al. 2009; Piersanti et al. 2009; Pakmor et al. 2012; Wang & Han 2012; Hoeflich et al. 2013; Tornambé & Piersanti 2013). Whether SNe Ia occur from one or likely both of the proposed progenitor systems, the rate of SNe Ia from each channel and observations of either the progenitor system or the post-explosion companion in supernova remnants (SNR) will help solidify the overall picture of SNe Ia. Observations of both SD and DD candidate systems can be found in Greiner et al. (1991), van den Heuvel et al. (1992), Rappaport et al. (1994), Kahabka & van den Heuvel (1997), Ruiz-Lapuente et al. (2004), González Hernández et al. (2009), Kerzendorf et al. (2009), Edwards et al. (2012), and Schaefer & Pagnotta (2012), and, in particular, Foley et al. (2014) and McCully et al. (2014).

Aside from the makeup of the progenitor system, the explosion mechanism is also a topic of debate. In the case of two WDs merging on a dynamical time-scale, the explosion is triggered by heat release during the merging process (Iben & Tutukov 1984; Webbink 1984; Benz et al. 1990; Lorén-Aguilar et al. 2009) (only possible in a DD system). Alternatively, the explosion can be triggered by compressional heat in an accreting WD when it approaches the Chandrasekhar mass limit ($\mathrm{M_{Ch}}$). The donor star can be a non-degenerate star or a tidally disrupted WD (Whelan & Iben 1973; Wang & Han 2012; Hoeflich et al. 2013). Scenarios with $\mathrm{M_{Ch}}$ explosions, whether originating from SD or DD progenitor systems, seem to be favored by observations of light curves and spectra, with some additional contribution from dynamical mergers (Saio & Nomoto 1985; Hoeflich & Khokhlov

1996; Saio & Nomoto 1998; Shen et al. 2012). Uncertainty about the progenitor system and explosion mechanism results in questions about the WD central density, total mass attained by the WD prior to the explosion, and the density profile of the WD just prior to the explosion.

The telltale indicator between the explosion scenarios is the central density of the WD at the time of the explosion. Within M_{Ch} models, the central density is an additional free parameter which depends mostly on the accretion rate and history (Sugimoto & Nomoto 1975; Nomoto et al. 1984; Thielemann et al. 1986; Brachwitz et al. 2000; Hoeflich 2006; Hoeflich et al. 2010; Seitenzahl et al. 2011). Slower accretion rates will lead to higher ρ_c because electron conduction is able to remove heat from the WD core and delay ignition of C in the core. In dynamical or violent mergers, the time scale for merging does not allow for cooling and ignition can be triggered at a much lower ρ_c.

Nuclear burning of a CO WD provides the energy to overcome the binding energy and provides the kinetic energy of the explosion. The time scales and the burning products depend mostly on the local density at the time of burning. Hydrodynamical instabilities may cause a redistribution of the burning products. Within the M_{Ch} channel, the most likely scenario involves delayed-detonation models (Khokhlov 1991; Yamaoka et al. 1992; Woosley & Weaver 1994; Gamezo et al. 2004; Röpke & Niemeyer 2007; Sim et al. 2013), i.e., models with a transition from a deflagration front to a detonation front (delayed-detonation transition; DDT). Independent of the explosion model, burning of a C/O mixture will produce regions of: iron group elements when burning reaches nuclear statistical equilibrium (NSE); layers of S/Si/Ar/Ca by incomplete burning; O/Mg/Ne as a product of explosive carbon burning; and some unburned outer layers. In the inner layers, NSE is achieved in all current explosion scenarios. However, only in M_{Ch} does burning occur under sufficiently high densities that electron capture can take place on hydrodynamical time scales which, in turn, shifts the peak of NSE from ^{56}Ni to stable isotopes of the iron group.

Observations during the photospheric phase allow investigation of the layers of incomplete burning and the ^{56}Ni region, which determine the peak brightness and Δm_{15}. However, observations of these regions provide hardly any information on the central region. The isotropic structure of the central region can be probed during the nebular phase by line profiles. To use line profiles we need an emission feature of iron that is unblended. Optical and most near-infrared (NIR) features are dominated by blends of multiple bound-bound transitions of various elements. However, the $1.644\,\mu$m feature of [Fe II] is a sensitive tool to separate stable and radioactive isotopes (Hoeflich et al. 2004; Motohara et al. 2006; Maeda et al. 2010; Sadler 2012; Penney & Hoeflich 2014). To produce an emission line, we need both the element and energy input by radioactive decay. After $200-300$ days, the energy deposition is dominated by positrons, which cannot excite the central low-velocity non-radioactive regions. The low-velocity emissivity produces "flat-topped" or "stubby" profiles which are a signature of M_{Ch} explosions without mixing. Up to about 200 days, the line profiles are peaked because gamma-rays contribute significantly to the energy input and excite the central, non-radioactive iron. Time evolution of the line profiles after $2-3$ years is sensitive to positron transport effects and, therefore, magnetic fields. Time evolution of the spectrum is needed in order to separate density, asymmetry in chemistry, and magnetic fields effects on the line profiles.

For the first time, a late-time evolutionary sequence of a SNe Ia is presented in the NIR that includes the $1.644\,\mu$m line of [Fe II]. Details of SN 2005df are presented in Sections 2 and 3. Reference models and rationale are outlined in Section 4. We develop general methods for comparing SNe Ia with the reference models as well as discuss the interpretation of the SN 2005df data in terms of our reference models and the implications of the analysis in Section 5. We compare the entire spectra between $0.82-1.8\,\mu$m to show the viability and uniqueness of the $1.644\,\mu$m [Fe II] feature. Finally, we discuss the implications of our results in Section 6.

2. OBSERVATIONS OF SN 2005DF AND DATA REDUCTION

SN 2005df was discovered on August 4, 2005, by Evans & Gilmore (2005a,b). Mid-infrared (MIR) observations of this SN Ia were previously analyzed by Gerardy et al. (2007), focusing on the [Co III] emission line at $11.89\,\mu$m and the [Ar II] and [Ar III] emission lines at $6.99\,\mu$m and $8.99\,\mu$m, respectively. Reviewing the initial published photometry and spectroscopy of SN 2005df, in addition to the range of distance estimates to the host galaxy NGC 1559, that analysis seemed consistent with a somewhat sub-luminous SN Ia (Gerardy et al. 2007). Light curve data for SN 2005df in the UV were analyzed by Brown et al. (2010) and Milne et al. (2010). The supernova's peak date in B-band was August 15, 2005. Milne et al. (2010) found that the light curve and Δm_{15} value of SN 2005df were consistent with a normal bright SN Ia, with a distance to the host galaxy larger than that used in the Gerardy et al. (2007) analysis.

For our analysis, observational epochs are given in relation to the estimated explosion date of August 2, 2005, to maintain consistency with Gerardy et al. (2007). Four epochs of late-time near-IR spectroscopy, ranging from 198 to 380 days after explosion, were observed using the Gemini Near Infrared Spectrograph (GNIRS) at the Gemini South Observatory. All spectra were taken in cross-dispersed (XD) mode, with the last observation also including spectra taken in long-slit (LS) mode. The spectra taken in the XD mode are spread out into different spectral orders; however, only orders $3-8$ have significant signal and are used in this analysis. The data from the 198 day observation were combined with the 199 day observation, because they lack accompanying standard star calibration images. The data were reduced following the standard procedure outlined in the Gemini IRAF package, with an exception for variance handling. Because of the low signal-to-noise ratio of these data, the variance was propagated for each step in the reduction using a custom script, assuming the original variance determined by the Gemini IRAF package and Poisson distribution of noise. This variance propagation deviates from the standard procedure during the NSCOMBINE and NSEXTRACT steps in the reduction.

The telluric standard stars we use for calibration pur-

poses are SAO 248743, used with the 198 day and 199 day observations, and SAO 249308, used with the 217 day and 380 day observations. Both of these stars have a spectral type of A0, with visual magnitudes of 8.3 mag and 7.3 mag, respectively (Ochsenbein et al. 2000). We use Kurucz' model for an A0V star along with the reduced telluric standard star spectra to determine the atmospheric and detector response corrections for the data (Kurucz 1993). The resolution for the theoretical standard star are at levels of 20 Å, 50 Å, and 100 Å in the $< 1.0\,\mu$m, $1.0 - 1.6\,\mu$m, and $> 1.6\,\mu$m regions, respectively. The 198 day and 199 day observations are corrected to be at the same relative fluxing as the 217 day and 380 day observations, and then normalized to the 217 day observation's [Fe II] peak at $1.644\,\mu$m. Absolute flux calibrating is not possible because photometric observations were not included in the observations. Fluxes have been normalized to the peak of the emission feature at $1.64\,\mu$m for this analysis.

3. PRELIMINARY ANALYSIS

The reduced spectra span a wavelength range of $\approx 0.8 - 2.4\,\mu$m. The spectra are dominated by broad emission features formed by line blends. Lines in the spectra are identified based on the models described in Section 4. Most of the identifiable emission is due to forbidden line transitions of iron and cobalt. Large regions of atmospheric absorption and low filter transmission obscure the spectra in the ranges $1.35 - 1.48\,\mu$m and $1.82 - 1.95\,\mu$m. The full spectra are split up into regions corresponding roughly to standard band-passes: $0.8 - 1.1\,\mu$m (see Figure 1), J at $1.1 - 1.35\,\mu$m (see Figure 2), H at $1.48 - 1.8\,\mu$m (see Figure 3), and K at $1.9 - 2.4\,\mu$m. The XD order 3 data are not shown because of the extremely low signal, especially in the 380 day observation, which prohibits any clear line identification in that region.

The XD orders 6, 7, and 8 data (see Figure 1 and Table 1) have features that are blends of many lines. Strong features are present at $\approx 0.86, 0.89, 0.95$ and $1.02\,\mu$m, which are dominated by forbidden transitions of the iron-group elements and sulfur. In addition, many forbidden and allowed transitions contribute both to the features and to the overall "quasi-continuum" flux. The spectral evolution reflects the transition from a cobalt- to an iron-dominated regime. We note that this region poses some problems related to the atmospheric corrections. The spectra of the telluric standard star flux reference, an A0V star (Kurucz 1993), includes features of strong and narrow Paschen lines of hydrogen. In combination with the low wavelength resolution in the telluric reference spectrum discussed in Section 2, the correction produces artifacts in the reduced spectra of SN 2005df. In the lower section of Figure 1, we show the correction factors applied for the three orders that make up this wavelength region. The overall sharp-edged shape of the strongest feature at $0.9 - 1.0\,\mu$m is likely caused by the rapid variations of the correction factors. Similarly, the narrow strong line at $\approx 0.951\,\mu$m is likely artificial. Its width corresponds to the detector resolution, $\approx 400\,\mathrm{km\,s^{-1}}$, and coincides in wavelength and size with a feature in the correction factors.

The XD order 5 data (see Figure 2 and Table 2) corresponds roughly to J band. In addition to the emission feature at $1.02\,\mu$m described above, a strong feature is

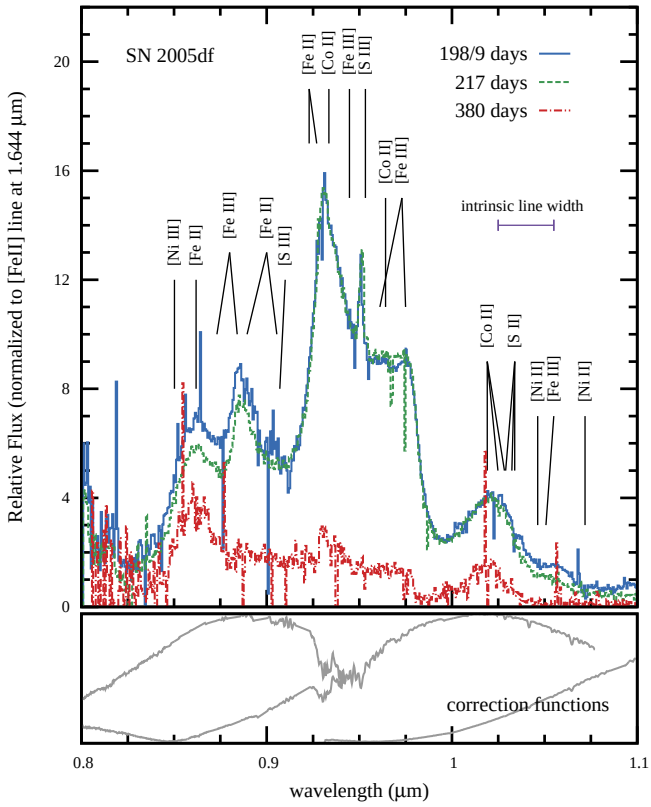

Figure 1. Spectra of SN 2005df in the region $0.8 - 1.1\,\mu$m at 198/9 days, 217 days, and 380 days. The spectrum is dominated by forbidden transition emission lines of iron, nickel, cobalt, and sulfur. Line identifications and the intrinsic line width are based on spectra from the reference model and its ^{56}Ni distribution, respectively, as discussed in Figure 4. Note that all of the features are heavily blended. In the lower plot, the relative correction factors are given for the atmosphere and the detector response for orders 8, 7, and 6.

apparent at $1.28\,\mu$m. Because the spectra are normalized to the [Fe II] line at $1.644\,\mu$m and this $1.28\,\mu$m feature is dominated by blends of [Fe II], it shows little evolution with time. Even though some of these emission lines are quite strong, the proximity of lines and the presence of the [Co III] line, which is decaying over timescales much shorter than that of the iron lines, make this feature difficult to use in probing the central chemical structure of the supernova.

The XD order 4 data and the LS data (see Figure 3 and Table 3) correspond roughly to H band. The dominant emission features are at $1.54, 1.64, 1.73$, and $1.82\,\mu$m. The second feature is dominated by one transition, an [Fe II] line at $1.644\,\mu$m, and shows very little evolution in shape over the observed epochs. Additional [Fe II] emission lines sit in both the blue and red wings of this main [Fe II] line, but their contributions are far enough out in the wings and low enough in strength that we can actually describe what is happening to that single emission line. The observed line center has a Doppler shift of less than $1200\,\mathrm{m\,s^{-1}}$ after correcting for the host galaxy's radial velocity. In contrast, the neighboring features are blends with significant evolution (Penney & Hoeflich 2014). The line center of the blended [Fe II]/[Co III] feature at $1.54\,\mu$m shifts toward the red (iron-line dominated side) in the 380 day spectrum, which is consis-

Table 1
Line identification for SN 2005df
(0.85 − 1.1 μm)

λ (μm)	Species	Term	J – J'
0.85020	[Ni III]	^{3}F – ^{1}D	2 – 2
0.86193	[Fe II]	a^{4}F – a^{4}P	9/2 – 5/2
0.87312	[Fe III]	a^{3}P – ^{3}D	2 – 3
0.88406	[Fe III]	a^{3}P – ^{3}D	2 – 2
0.88944	[Fe II]	a^{4}F – a^{4}P	7/2 – 3/2
0.90544	[Fe II]	a^{4}F – a^{4}P	7/2 – 5/2
0.90711	[S III]	^{3}P – ^{1}D	1 – 2
0.92291	[Fe II]	a^{4}F – a^{4}P	5/2 – 3/2
0.92701	[Fe II]	a^{4}F – a^{4}P	3/2 – 1/2
0.93357	[Co II]	a^{3}F – b^{3}F	4 – 3
0.94467	[Fe III]	^{H} – a^{1}G	5 – 4
0.95332	[S III]	^{3}P – ^{1}D	2 – 2
0.96113	[Fe III]	^{H} – a^{1}G	4 – 4
0.96418	[Co II]	a^{3}F – b^{3}F	3 – 2
0.97045	[Fe III]	^{3}H – ^{1}I	6 – 6
1.0191	[Co II]	a^{3}F – b^{3}F	4 – 4
1.0248	[Co II]	a^{3}F – b^{3}F	3 – 3
1.0280	[Co II]	a^{3}F – b^{3}F	2 – 2
1.0290	[S II]	^{2}D^o – ^{2}P^o	3/2 – 3/2
1.0323	[S II]	^{2}D^o – ^{2}P^o	5/2 – 3/2
1.0339	[S II]	^{2}D^o – ^{2}P^o	3/2 – 1/2
1.0463	[Ni II]	^{2}F – ^{4}P	7/2 – 5/2
1.0507	[Fe III]	a^{3}P – ^{3}D	0 –1
1.0718	[Ni II]	^{2}D – ^{4}F	5/2 – 7/2

Table 2
Line identification for SN 2005df
(1.1 − 1.35 μm)

λ (μm)	Species	Term	J – J'
1.1163	[Fe II]	a^{4}H – b^{2}G	11/2 – 9/2
1.1363	[Ni II]	^{2}F – ^{1}D	5/2 – 3/2
1.1616	[Ni II]	^{2}D – ^{4}F	3/2 – 5/2
1.2326	[Ni II]	^{2}F – ^{4}P	5/2 – 5/2
1.2489	[Fe II]	a^{6}D – a^{4}D	7/2 – 5/2
1.2570	[Fe II]	a^{6}D – a^{4}D	9/2 – 7/2
1.2707	[Fe II]	a^{6}D – a^{4}D	1/2 – 1/2
1.2791	[Fe II]	a^{6}D – a^{4}D	3/2 – 3/2
1.2946	[Fe II]	a^{6}D – a^{4}D	5/2 – 5/2
1.2981	[Fe II]	a^{6}D – a^{4}D	1/2 – 3/2
1.3209	[Fe II]	a^{6}D – a^{4}D	7/2 – 7/2
1.3281	[Fe II]	a^{6}D – a^{4}D	3/2 – 5/2

completely faded in the 380 day spectrum. The strongly blended [Fe II]/[Fe III]/[Co III]/[Ni II]/[Ni IV] feature at 1.82 μm, with wings starting just at the red edge of Figure 3, does not seem to change between the three epochs, but these lines are just at the edge of a low transmission region due to filter overlap and atmospheric corrections. The small variation in this feature is indicative of stable isotopes, namely iron and nickel, with the latter being observed as [Ni II] and [Ni IV] in the MIR as isolated lines in Gerardy et al. (2007) and Telesco et al. (2014).

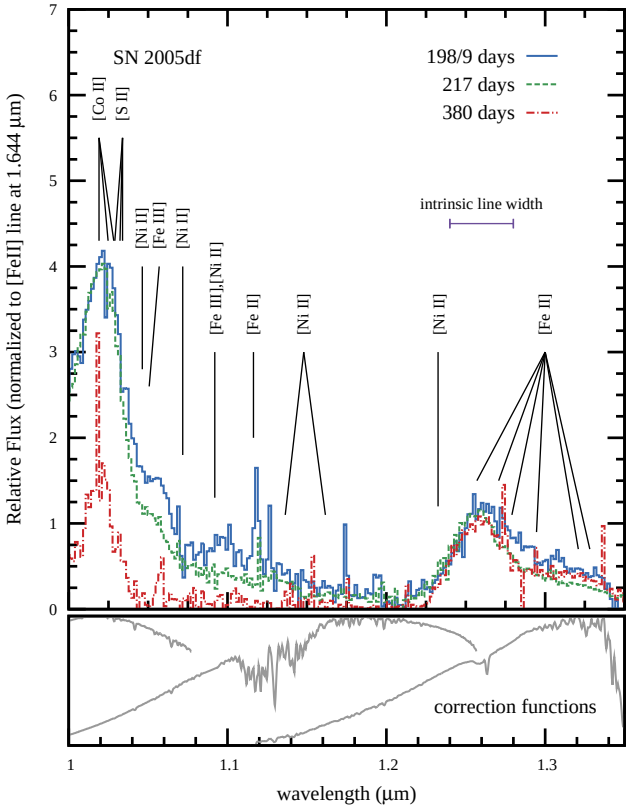

Figure 2. Same as Figure 1 but for the region 1.1 − 1.35 μm. Note that all of the features are heavily blended. In the lower plot, the relative correction factors are given for the atmosphere and the detector response for orders 7, 6, and 5.

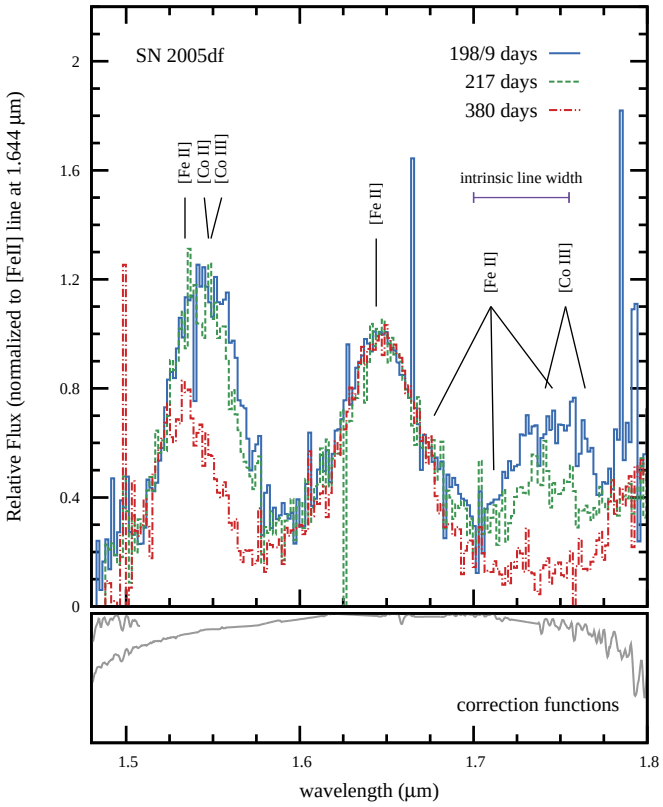

Figure 3. Same as Figure 1 but for the region 1.48 − 1.8 μm. In the lower plot, the relative correction factors are given for the atmosphere and the detector response for orders 5 and 4. Note the small variability of the correction factor between 1.6 − 1.7 μm.

tent with the cobalt line fading but the iron line remaining strong. The blended [Co III] feature at 1.74 μm has

Over the entire spectral range, the extracted spectra show evolution of cobalt emission lines but minimal evo-

Table 3
Line identification for SN 2005df ($1.5-1.8\,\mu$m)

λ (μm)	Species	Term	J – J'
1.5339	[Fe II]	$a^4F - a^4D$	9/2 – 5/2
1.5474	[Co II]	$a^5F - b^3F$	5 – 4
1.5488	[Co III]	$a^2G - a^2H$	9/2 – 9/2
1.6440	[Fe II]	$a^4F - a^4D$	9/2 – 7/2
1.6773	[Fe II]	$a^4F - a^4D$	7/2 – 5/2
1.7116	[Fe II]	$a^4F - a^4D$	5/2 – 3/2
1.7413	[Co III]	$a^2G - a^2H$	9/2 – 11/2
1.7454	[Fe II]	$a^4F - a^4D$	3/2 – 1/2
1.7643	[Co III]	$a^2G - a^2H$	7/2 – 9/2
1.8099	[Fe II]	$a^4F - a^4D$	7/2 – 7/2
1.8119	[Fe II]	$a^4D - a^4P$	7/2 – 5/2
1.8203	[Fe III]	$^1I - ^3H$	6 – 6
1.8214	[Co III]	$a^4P - a^2P$	3/2 – 1/2
1.8932	[Ni IV]	$^4P - ^2P$	3/2 – 3/2
1.8958	[Ni II]	$^2D - ^2P$	3/2 – 3/2

lution of iron emission lines, consistent with the decay from cobalt to iron. The region of most interest for our analysis is around $1.5-1.8\,\mu$m, which includes a mixture of both iron and cobalt emission lines. In Section 5.3, the evolution of the [Fe II] emission line at $1.644\,\mu$m is used to put limits on the central density of the WD and the strength of the magnetic field in the progenitor by comparing with models produced by Hoeflich and Penney (Penney 2011; Penney & Hoeflich 2014).

4. MODELS

Based on detailed spherical models for supernovae discussed below, we analyze the spectral features of SN 2005df and their evolution. The simulations are consistent with respect to the explosion, light curves, and spectra. We emphasize that the time evolution of the NIR spectrum follows without additional free parameters, given the initial WD model and parameterized properties for nuclear burning.

4.1. *Methods*

For the calculations of explosions and spectra, we use our code for radiation hydrodynamics (HYDRA; Hoeflich 1990, 1995, 2002, 2009) which solves for the hydrodynamics using the explicit Piecewise Parabolic Method (PPM; Colella & Woodward 1984), detailed nuclear and atomic networks (Kurucz 1994; Hoeflich 1995; Seaton 2005; Cyburt et al. 2010), transport for low-energy and gamma-transport photons and positrons by variable Eddington Tensor solvers and Monte Carlo Methods (Stone et al. 1992; Hoeflich et al. 1993; Mihalas & Mihalas 1999; Hoeflich 2002, 2009; Penney & Hoeflich 2014). For this study, atomic data for forbidden line transitions have been updated using Quinet et al. (1996), Quinet (1996), Quinet (1998), De et al. (2010), Friesen et al. (2014), Kramida et al. (*NIST Atomic Spectra Database*; 2014), and van Hoof (*The Atomic Line List*; 2014).

4.2. *Model Selection Criteria*

In the simulations, we use a spherical, delayed detonation model. Spherical geometry implies suppression of mixing during the deflagration phase. Varying the amount of burning prior to the DDT produces a wide range of values for ^{56}Ni mass and the corresponding brightness. It shifts the characteristic chemical pattern in velocity space (see Figure 3 in Hoeflich 2002). The explosion models are based on a WD of solar metallicity with a main sequence mass of $7\,M_\odot$, 7p0z22. Within spherical DDT-models, the amount of ^{56}Ni produced depends mainly on the amount of burning prior to the DDT. This class of models have previously been used with success in reproducing the optical light curves, IR light curves, and spectra of a Branch-normal and several sub-luminous SNe Ia, in addition to the statistical properties of the SNe Ia class (Hoeflich et al. 2002; Howell et al. 2006; Marion et al. 2006; Quimby et al. 2007; Hoeflich et al. 2010; Maund et al. 2010; Patat et al. 2012; Marion et al. 2009; Sim et al. 2013; Dessart et al. 2014). Guided by the 5p0z22-series of models in Hoeflich et al. (2002) with M_V between -17.21 to -19.35, we choose a model that produces about $0.60\,M_\odot$ of ^{56}Ni, which is consistent with SN 2005df. For our WD, 7p0z22, using an initial central density of $0.9\times10^9 g/cm^3$, the model peaks at an absolute magnitude of $M_B=-19.29$ mag and has decline ratios of $\Delta m_{15}(B)=1.14$ mag and $\Delta m_{15}(V)=0.61$ mag. These values are comparable to the observed values for SN 2005df of $\Delta m_{15}(B)=1.2$, $\Delta m_{15}(V)=0.63$ mag, and $M_B=-19.23(\pm0.10)$, assuming a distance modulus of $\mu=31.81$ as in Milne et al. (2010).

For this study, the initial central density of the WD, ρ_c in units of $10^9 g/cm^3$, and initial magnetic field have been varied between $0.5-4.0$ and $10^0-10^9 G$, respectively, to provide a range of models to analyze the NIR spectra of SN 2005df. Note that the resulting light curve variations are small, $\delta(M_V)\approx\pm0.04$ mag, $\delta(\Delta m_{15}(B))\approx\pm0.07$, and $\delta(\Delta m_{15}(V))\approx\pm0.03$ (Hoeflich 2006; Hoeflich et al. 2010), and can be ignored.

5. RESULTS

5.1. *Effects of Central Density*

Because all of the reference models are constructed with a very similar density at which the DDT occurs, the abundance profiles of ^{56}Ni look identical in the outer regions of velocity-space, as can be seen in Figure 4. However, the interior profile varies dramatically, with radioactive nickel providing less and less of a low-velocity contribution with increasing central density. We note that this velocity profile does not mean the emission line widths will be on the order of $10,000\,\mathrm{km\,s^{-1}}$. Assuming a spherical distribution of material, the line widths will actually be significantly narrower because of projection effects.

As the central density increases, there is a larger fraction of material at high enough density during the deflagration for electron capture to occur and produce sizable amounts of stable ^{58}Ni (Hoeflich 2006). This "hole" in the radioactive material does not contribute to the emission features in the nebular spectrum until very late times when the positrons have become non-local. Figure 5 shows the size of the ^{58}Ni hole increasing with ρ_c, and this corresponds to a broadening of the nickel, cobalt, and iron emission lines.

5.2. *Benefits of the H-band Region*

As can be seen from the SN 2005df spectra in Figures 1-3, there are significant overlapping emission lines

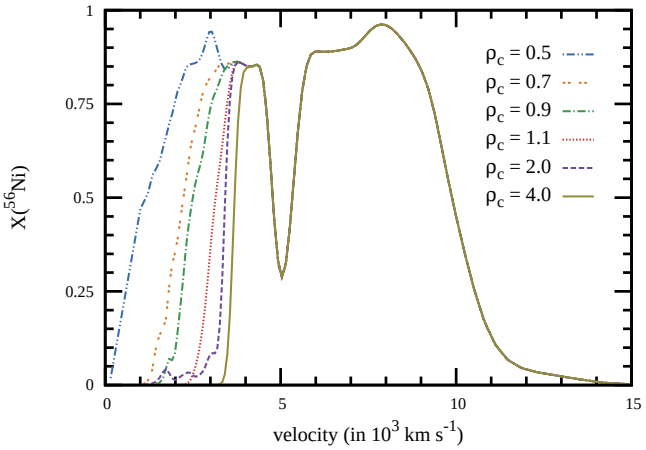

Figure 4. The abundance of ^{56}Ni at $t = 0$ as a function of the expansion velocity for models with various initial central densities ρ_c of the WD (in $10^9\,\mathrm{g\,cm^{-3}}$). The lack of ^{56}Ni is due to electron capture which shifts the NSE to stable isotopes of iron group elements. Thus, the size of the ^{56}Ni hole increases with ρ_c. The dip at $5000\,\mathrm{km\,s^{-1}}$ is an artifact of spherical delayed detonation models and caused by the strong reflection wave produced by the DDT.

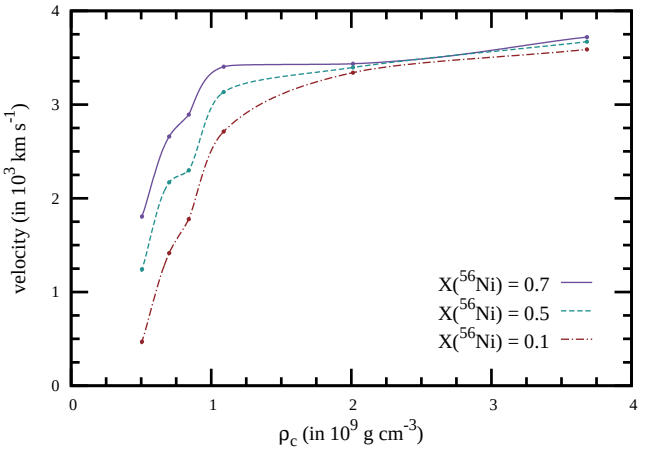

Figure 5. Size of the ^{56}Ni hole in velocity space as a function of ρ_c. Here the edge of the hole is defined by abundance levels of 0.7, 0.5, and 0.1.

contributing to most of the features seen in the NIR. The "cleanest" feature in the entire observed region is the [Fe II] line at $1.644\,\mu$m, whose closest satellite line with moderate strength is $0.333\,\mu$m away from line-center. The entire H-band region from $1.5 - 1.8\,\mu$m can effectively be modeled using just the contributions from the strongest emission lines listed in Table 3. In this analysis, we will find which of the references models best fits with the data by considering only the $1.644\,\mu$m line. The other NIR features come out naturally.

5.3. *Model Comparison*

By 200 days after the explosion the energy deposition transitions from gamma-dominated to positron-dominated. Unlike gamma rays, whose path is not affected by a magnetic field embedded in the ejecta, the positrons are very much dependent on whether or not there is a magnetic field present and the strength of that field. With no magnetic field, positrons deposit energy locally early on, and we would expect any central region of ^{58}Ni to not contribute to the observed emission lines, providing a "flat-topped" or "stubby" line profile. However, with time, positrons are able to travel throughout the central non-radioactive region, and we transition from seeing a flat-topped profile to a peaked profile, with the line evolving most quickly in the wings where the higher-velocity material is able to become non-local first. A more in-depth discussion of line evolution with magnetic fields is presented in Section 5.5.

5.4. *Central Density Fitting*

As discussed in Section 5.1, the distribution of iron group elements in the central regions depends on the initial central density of the WD. Therefore, the shape of the line profile, specifically the line width, is sensitive to measuring ρ_c. Our procedure for finding the line width (LW) of the $1.644\,\mu$m line is as follows:

1. subtract the free-free continuum produced by the models, re-normalizing to the $1.644\,\mu$m peak, to give the line profile a zero-point;

2. pick fixed y-value points (denoted H in plots) in increments of 0.1 or smaller, as signal-to-noise of the data allow;

3. for each of the chosen y-values, the corresponding velocity x-values are obtained using a linear regression through adjacent data points, with multiple resolution elements used in the case of the data to decrease the effects of noise;

4. for each epoch and magnetic field strength, measure LW from the $+x$-value to the $-x$-value for each of the chosen y-values.

Because of this treatment, line evolution is determined only by drop-out in the wings or core and does not include changes in the total line flux. This representation allows for direct comparison to our observational data, in which total flux could not be measured. Figure 7 shows the observational data and the velocity x-values we obtain for each y-value.

The continua produced by the reference models are at levels of 9%, 7%, and 2% of the line-height for the 198/9 day, 217 day and 380 day epochs, respectively. These modeled continua are also taken to zero-point the SN 2005df data. However, this zero-point uncertainty may add additional error to our measurements that will systematically increase the measured LW. A maximum possible continuum can be determined using the minimum observed flux in the corresponding wavelength range (Figure 3). Using this method, the systematic errors in the continua are less than 15%, 16%, and 12% for the 198/9 day, 217 day, and 380 day observations, respectively, before the modeled continua are removed. The systematic error estimates in LW are obtained as follows: use the continuum error to determine the maximum adjusted H'; use the original H values to interpolate new velocity values at H'; obtain a new estimate for LW', where the systematic uncertainties are given by $LW' - LW$. For our observations, comparing $H = 0.6$ and H', we get $H' = 0.624$, 0.636, and 0.64 for

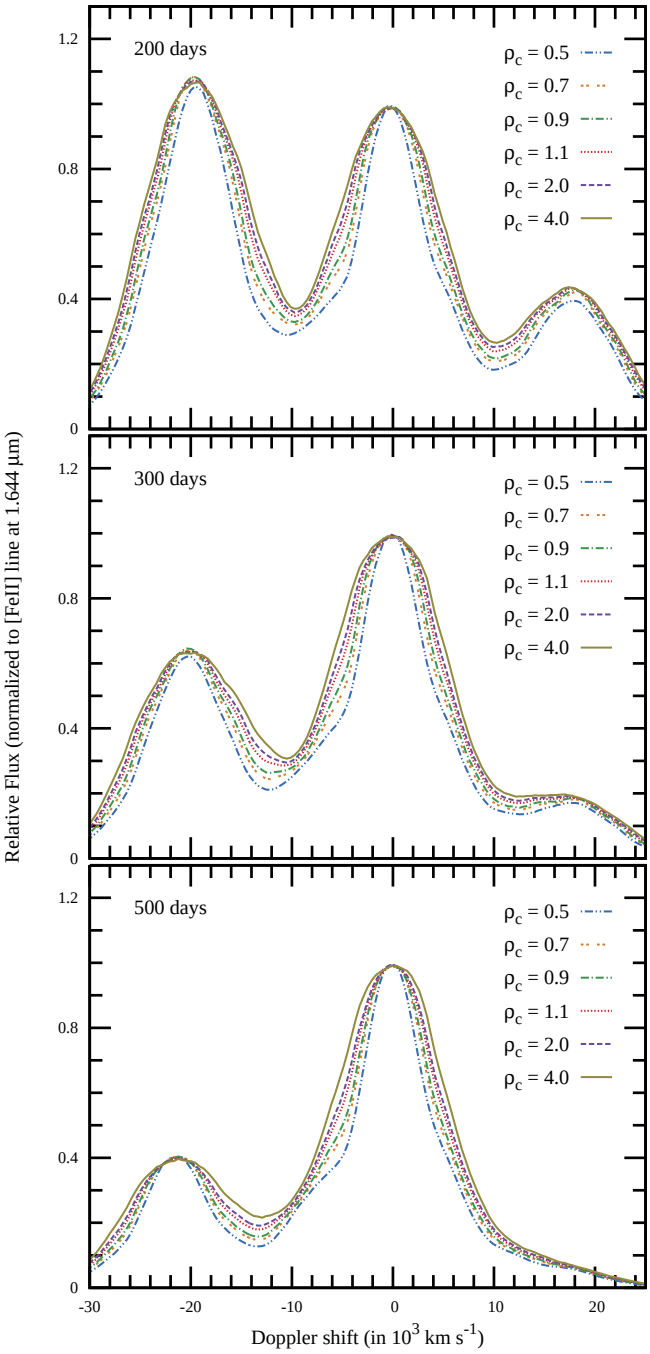

Figure 6. Time evolution of the [Fe II] emission line at 1.644 μm in velocity space of our reference models with $B = 10^0$ G. In wavelength this region spans $1.48 - 1.78\,\mu$m. The strong neighboring features on the blue and red side are produced by blends of [Fe II]/[Co III] and [Co III], respectively (see Table 3).

the three epochs. The systematic error due to continuum uncertainty will affect the line width at a maximum level of $600\,\mathrm{km\,s^{-1}} - 700\,\mathrm{km\,s^{-1}}$, with the 217 day observation having the largest possible effect.

One of the advantages of the method we have developed is that there is not one specific measurement that must be made. The line width can be measured at a variety of different H-values to ensure that the results found are consistent. Noise in the data in small wavelength regions will not affect the overall result. The y-value of 0.6 has been chosen for display in Figures 8 and 12 even though each y-value we tested produces very similar results. At 0.6 the level of contamination from the neighboring satellite lines to 1.644 μm [Fe II] line, which increases with decreasing H, is small. Similarly, the uncertainty when finding the corresponding velocity x-values, which increase with increasing H, is small because of the slope of the line in that region.

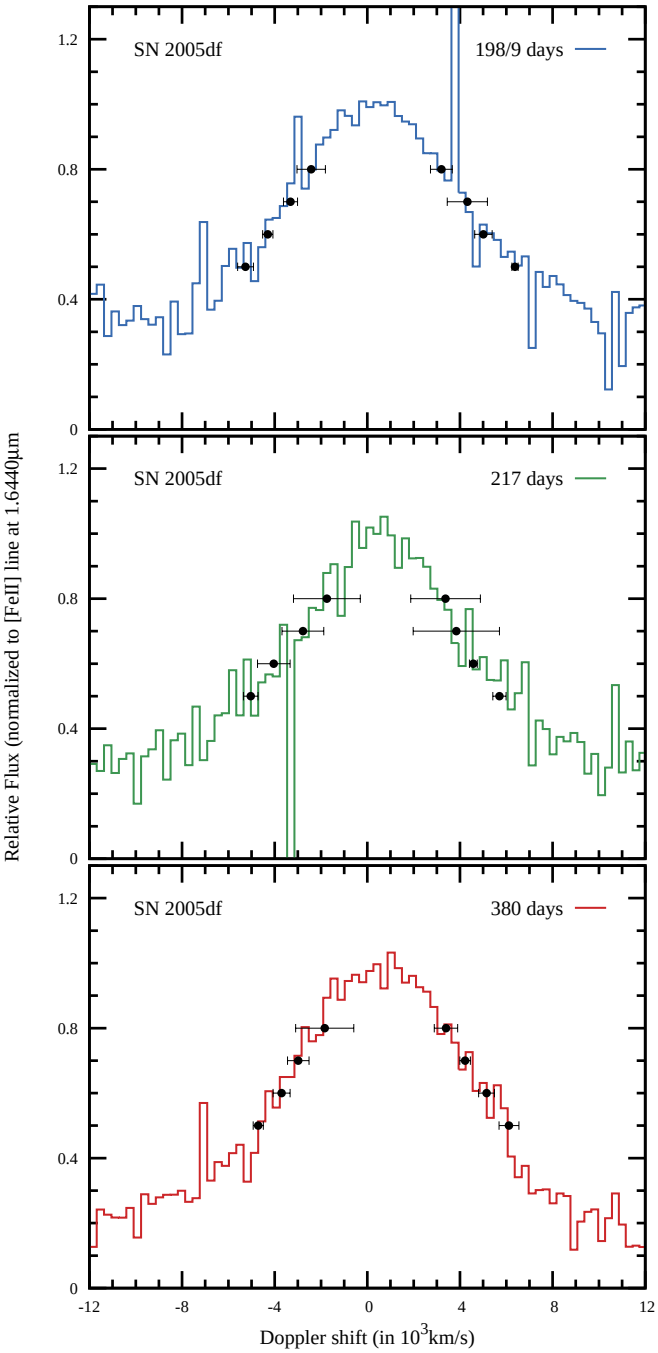

Figure 7. Observed spectra at 198/199 days, 217 days, and 380 days for the [Fe II] 1.644 μm line. The plot shows the velocity approximations at different heights ($0.5 \leq H \leq 0.8$) overlaid on the actual data. These values are the ones used to determine line width for the observational data. We limit the range for H because the wings of this feature are contaminated by neighboring iron and cobalt emission lines.

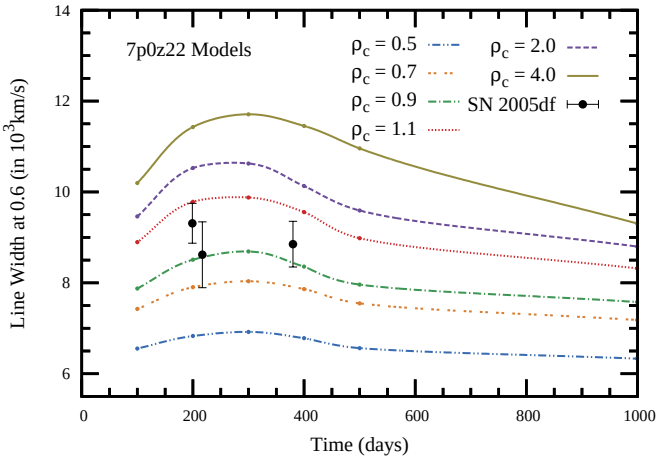

Figure 8. Comparison between *LW* observed for SN 2005df and our reference models at $H = 0.6$ for the [Fe II] emission line at 1.644 μm. The errors bars given are produce by the noise in the data (see text). Good agreement with the SN 2005df data can be obtained for models with ρ_c between 0.9 and 1.1.

Using *LW* to determine the initial central density of the WD for SN 2005df, we find that ρ_c(SN 2005df) = $0.9(\pm 0.2)$ (in $10^9\,\mathrm{g\,cm^{-3}}$). The systematic error due to continuum uncertainties is just over the 1σ-level but can only make *LW* narrower and, therefore, the central density lower. This central density is high enough that SN 2005df would have a moderately-sized region of stable ^{58}Ni at low velocity, however not enough to produce the characteristic "flat-topped" line profiles seen in SN 2003du and SN 2003hv. The best-fit reference model is shown plotted with the SN 2005df data in Figure 9. The line-center for the [Fe II] line at 1.644 μm is shifted by less than $1200\,\mathrm{km\,s^{-1}}$. The main feature is very well reproduced in line profile both in the core and wings of the line. There are some discrepancies in the relative fluxes for the neighboring features around $-20,000\,\mathrm{km\,s^{-1}}$ (corresponding to 1.54 μm) and $18,000\,\mathrm{km\,s^{-1}}$ (corresponding to 1.74 μm). However, these may be attributed to the treatment of super-levels in the reference models or in the simplistic treatment of continuum subtraction.

5.5. *Effects of Magnetic Fields*

By looking at the initial line profile and the evolution, we can put a lower limit on the strength of a magnetic field embedded in the SN ejecta. Large magnetic fields embedded in the SN ejecta keep the energy deposition of the positrons local longer than in a $B = 0$ G model, because the positron path-length increases dramatically. In order to probe this effect, we have included a range of field strengths for a magnetic field embedded in the SN ejecta: $B = 10^0$ G, 10^3 G, 10^4 G, 10^6 G, and 10^9 G.

For this analysis, the model data are averaged over angle for each epoch and progenitor field strength, although discussion of the effect of orientation is presented below and shown in Figure 11. In order to look at the effects of magnetic field strength, a low-ρ_c and a high-ρ_c case are shown in Figure 10 at 300 days (top panel) and 500 days. Although the energy deposition is dominated by positrons at 300 days, the positrons are still localized and even the most extreme magnetic field, $B = 10^9$ G, only affects the flux to a minor extent. By 500 days, the magnetic field effect on the flux is within a measurable range for the high-ρ_c spectrum, with the extreme $B = 10^9$ G spectrum retaining its "flat-topped" profile.

The morphology of the magnetic field can also affect the line profile shape and evolution; however, only models with a dipole field are considered here (Penney & Hoeflich 2014). Additionally, there is an effect of the viewing angle with respect to the orientation of the magnetic field's dipole, which impacts the line pro-

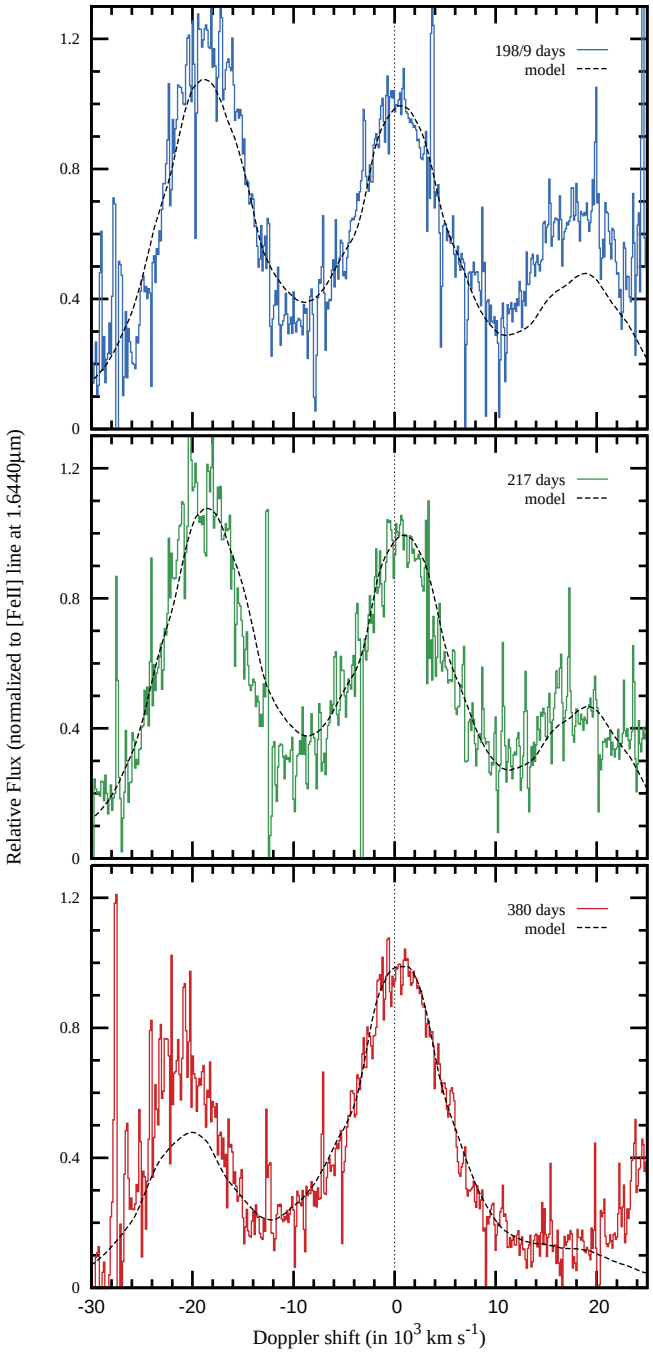

Figure 9. Comparison between spectra of SN 2005df and the reference model with $\rho_c = 0.9$ and $B = 10^0$ G. Note the discrepancies of the relative flux in the neighboring features which may be attributed to uncertainties in the continuum or the model atoms (see text).

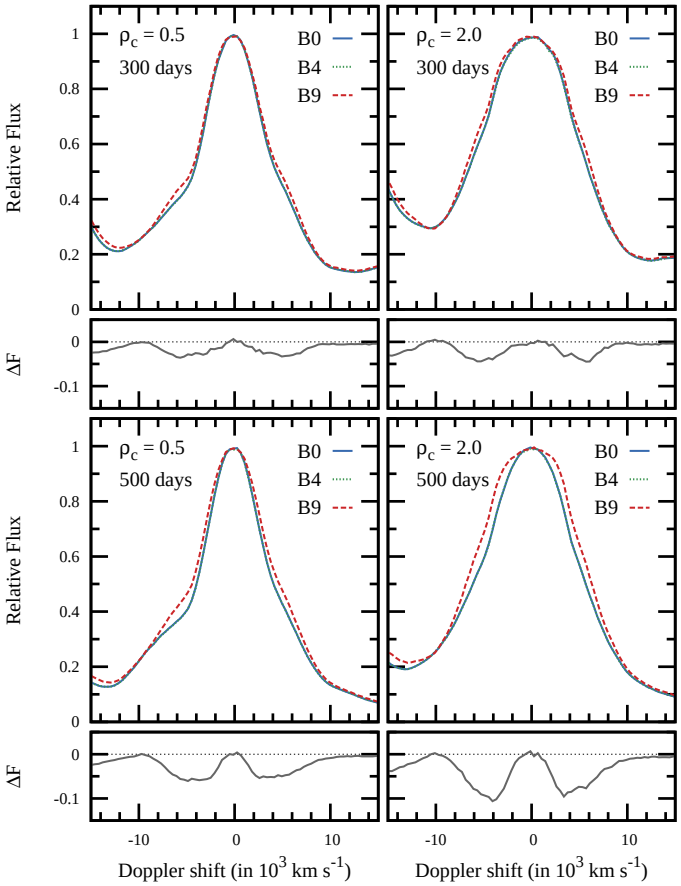

Figure 10. Influence of the strength of the magnetic field on the angle-averaged line profile of the 1.644 μm [Fe II] line at 300 days and 500 days. Below each plot, the difference in line profile is shown between $B = 10^0$ G (B0) and $B = 10^9$ G (B9). Positrons are responsible for the energy input during late times t. At 300 days, the influence of B is smaller than a shift of 1000 km s^{-1} in all of the reference models. At 500 days, the influence of B on the core of the line ($H = 0.6$) for the low and high density model is ≈ 750 km s^{-1} and ≈ 1750 km s^{-1}, respectively. This puts the magnetic field effect close to the resolution limit of our measurements for SN 2005df, assuming a relatively low initial central density as found in Section 5.4. Note that the wing is determined by high velocity ^{56}Ni justifying our choice of $H = 0.6$ to measure ρ_c.

file shape and evolution. In most of the reference models, the difference between the flux when viewed from a polar orientation versus an equatorial orientation is smaller than the resolution limit for our SN 2005df observations and will be negligible for our purposes. In cases of large central densities, however, the difference between flux for the normalized line can be as large as $\Delta F = 0.2$, and this effect should be considered along with other variations in the line profile. Two cases are shown in Figure 11, both at 500 days: $\rho_c = 0.9 \times 10^9$ g cm^{-3} with $B = 10^9$ G and $\rho_c = 4.0 \times 10^9$ g cm^{-3} with $B = 10^9$ G.

A rough cut of central densities can be made using line widths. However, even by $200 - 300$ days, a strong magnetic field keeps LW larger when compared to the $B = 0$ G model. With the SN 2005df observations, the two effects are indistinguishable because of the noise in the data and the limited epochs of observation, as can be seen in Figure 12. A non-zero magnetic field is only favored by a 1σ-level. Figure 12 shows that an observation at 400 days post-explosion or later, in addition to an early nebular phase observation, is needed in order to obtain both ρ_c and magnetic field strength.

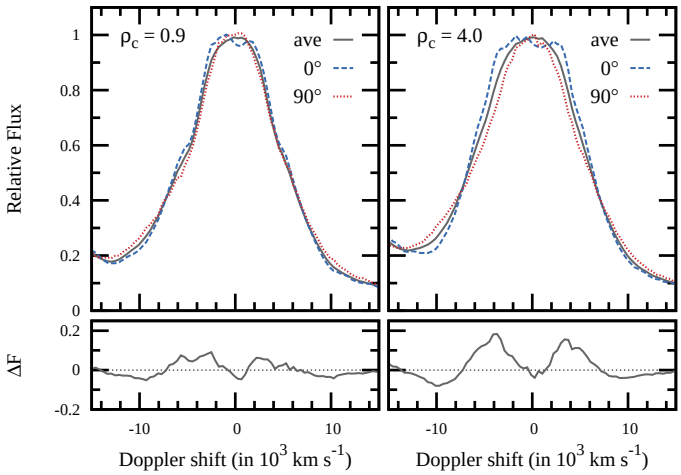

Figure 11. Same as Figure 10 but showing the influence of the observation angle. Orientation effects remain small for $\rho_c = 0.9$ even at 500 days.

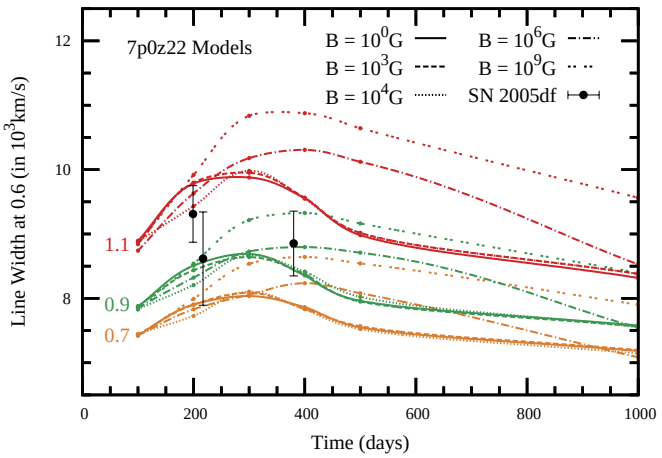

Figure 12. Same as Figure 8 but for a reduced sample with magnetic field effects included. For low ρ_c, B effects remain small. The late time observation of SN 2005df favors $B \approx 10^6$ G by a 1σ level only.

5.6. *Overall Spectral Comparison for the Wavelength Range* $0.8 - 1.35\,\mu$m

In this section we compare the short wavelength region, $0.8 - 1.35\,\mu$m, of SN 2005df with our best-fit reference model (Figure 13). The fluxes have been normalized to the 1.644 μm [Fe II] line without further tuning. Most of the features seen in SN 2005df can be reproduced, which allows for the identification of the main spectral features as given in Tables 1 and 2. At both 200 days and 400 days, the spectra are dominated by iron group elements, and evolution of the spectra can be understood by the transition from a cobalt-dominated to an iron-dominated regime. This is evident by the rapid evolution of the broad feature at 0.95 μm compared to the slow changes in the iron-dominated features at 0.86 μm, 1.03 μm, and 1.26 μm, which are produced by blends of [Fe II], [S II], and [Fe II], respectively. Both the width and flux ratios of features are reproduced in the

model. We note, however, that each of the main features is strongly blended, emphasizing the uniqueness of the [Fe II] emission line at 1.644 μm used in the previous sections for central density and magnetic field strength analyses.

By 200 days after explosion, the envelope is mostly transparent. Most of the radioactive ^{56}Ni and ^{56}Co has decayed to ^{56}Fe, and stable nickel and iron are fully exposed. The models show, and we want to emphasize, that normalization of spectra to this line allows us to separate whether features are dominated by stable or unstable isotopes.

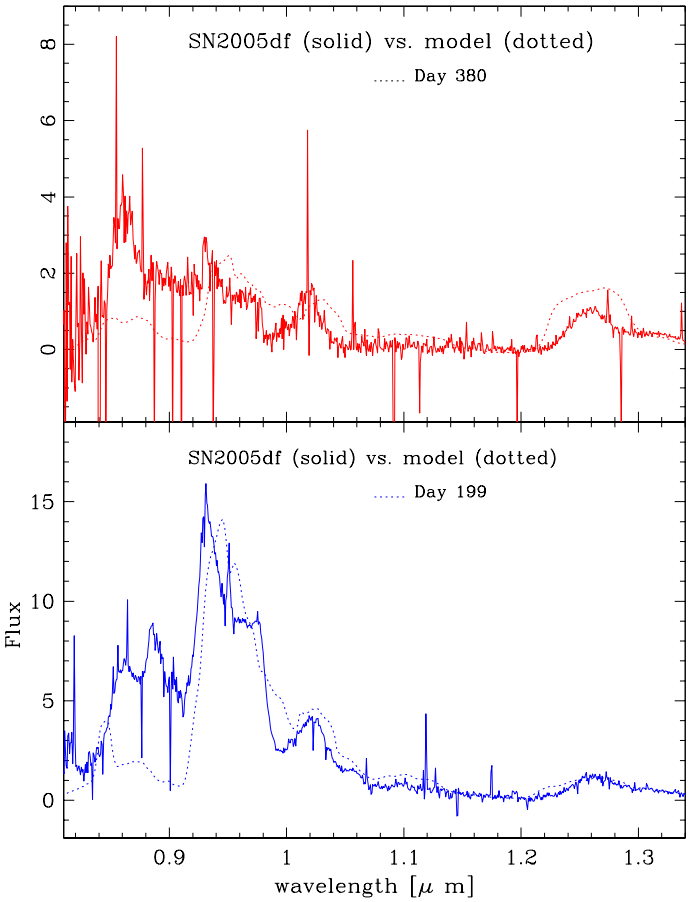

Figure 13. Same as Figure 9 but for the short wavelength range. The fluxes have been normalized to the 1.644 μm [Fe II] line.

Some discrepancies are clear. The flux between below 0.92 μm is too low by a factor of 3, and a narrow feature is present at 0.95 μm with a width corresponding to the instrumental resolution of $\approx 400\,\mathrm{km\,s^{-1}}$. The problem may be related to the use of super-levels and the lack of atomic data with the reference model. However, tests with various cross sections from literature produce changes of only $20-30\%$. Alternatively, the inconsistency may be related to the atmospheric corrections during data reduction. As discussed in Section 2, we use the fluxes calibrated by the energy distribution of an A0V standard star with a resolution of 20 Å to 50 Å, which is larger than the detector resolution in the wavelength range shown in Figure 13. Additionally, A0V stars have strong lines in the Paschen series in this region, and the correction factors vary by ≈ 2, which may produce an overcorrection of the SN 2005df flux.

Moreover, a strong, narrow feature at 0.95 μm is unexpected based on the models and would imply a component with high emissivity in a very localized region, $\approx 400\,\mathrm{km\,s^{-1}}$, in the envelope. In the line list, this feature could be [S III], but it is difficult to imagine a scenario where sulfur can be excited at high levels without a corresponding narrow feature in cobalt. Therefore, we regard the atmospheric correction as the likely source, especially considering the coincidence of the feature with a Paschen line in the A0V telluric standard star.

5.7. *Implications of the Central Density for the Possible Progenitor and Explosion Scenario of SN 2005df*

As discussed in Section 1, different progenitor systems and explosion scenarios can be distinguished by ρ_c. The pressure in the WD is dominated by a degenerate electron gas. With increasing density, this Fermi gas becomes increasingly relativistic degenerate, and ρ_c increases rapidly when approaching M_{Ch}. As a consequence, ρ_c is a steep function of the WD mass, M_{WD} (see Figure 14). We note that the equation of state determines the M_{Ch} for the WD and depends on the metallicity, composition, and accretion. However, in practice, a WD cannot reach this limit because densities get high enough that the time scales for electron capture become shorter than the hydrodynamical time scales, which reduces pressure in the WD core and causes an accretion induced collapse (AIC). In Figure 14, our reference mass for M_{Ch} is taken when $\rho_c \approx 7.0$ (in units of $1\times10^9\,\mathrm{g\,cm^{-3}}$) and assumes low accretion rates.

For SN 2005df, we obtain $\rho_c = 0.9(\pm0.2)$ (in $10^9\,\mathrm{g\,cm^{-3}}$) in Section 5.4. Our systematic error due to continuum uncertainty is at about the 1σ-level. Despite the rather large error range in ρ_c, the steep dependence of ρ_c on the mass of the WD puts a strong constraint on M_{WD}(SN 2005df) $= 1.313(\pm0.034)\,M_\odot$ with a 2σ confidence and systematic error less than $0.04\,M_\odot$. Mixing of ^{56}Ni will increase the central emission component, thus decreasing the line width of the 1.644 μm line and mimicking a lower central density. Therefore, ρ_c(SN 2005df) and the corresponding M_{WD}(SN 2005df) should be taken as lower limits. Because dynamical mergers occur in a wide range of masses, they are unlikely progenitors for SN 2005df.

For M_{Ch} scenarios, the explosion is triggered by compressional heating due to increasing mass by accretion from the companion star. To first order, ρ_c is determined by the balance of this heating with cooling by conduction. The ρ_c(SN 2005df) found in our analysis implies an upper end for the rate of H-accretion. As discussed in Section 1, higher accretion rate can be achieved for accretion of He and C.

Electron capture takes place in the center of WDs when they approach M_{Ch} prior to the explosion, during the convective "smoldering" phase. The Urca process, which involves neutrino emission as a consequence of electron capture, was thought to cool the WD center and delay the onset of explosive C burning (Paczyński 1972; Barkat & Wheeler 1990). This would mean that M_{Ch} scenarios should transition into an explosion only at central densities in excess of $3\times10^9\,\mathrm{g\,cm^{-3}}$. However, this

notion was recently debated. It was noted that neutrino emission also has the opposite effect of slowing down the convection and thus heating the core (Stein et al. 1999). Cooling and heating due to the Urca process may cancel out (Stein & Wheeler 2006), and our results lend support to this conclusion.

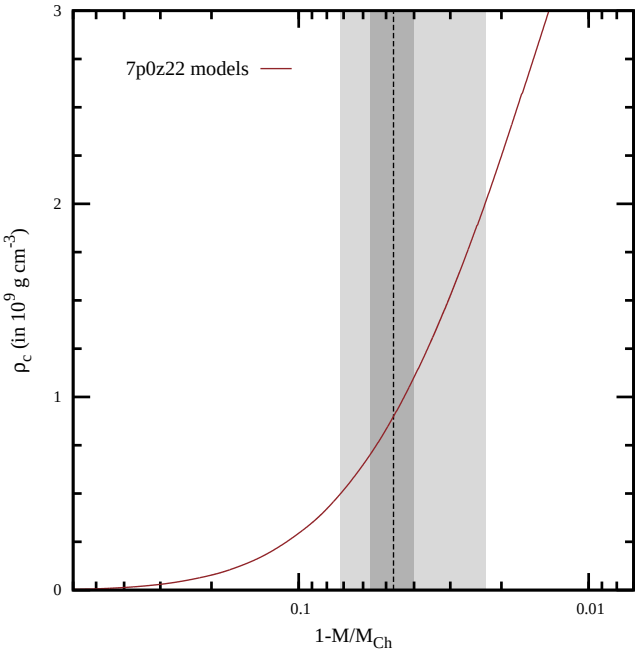

Figure 14. Central density ρ_c as a function of the progenitor. There is a rapid increase of ρ_c towards M_{Ch}. Therefore we show ρ_C as a function of $1-M_{WD}/M_{Ch}$ (mass fraction away from M_{Ch}). In addition, the best-fit central density for SN 2005df is given, with the dotted line showing the corresponding $1 - M_{WD}/M_{Ch}$. The dark and light gray areas denote the regions with 1σ and 2σ probability which span $\rho_c = 0.7 - 1.1$ and $\rho_c = 0.5 - 2.0$ (in units of 10^9 g cm^{-3}), respectively.

6. CONCLUSIONS

We have shown the time evolution of the NIR spectrum of SN 2005df, specifically focusing on the [Fe II] emission line at 1.644 μm. We found that this line provides a unique tool to analyze near-infrared spectra. Normalization to this line allows separation of features produced by stable versus unstable isotopes of iron group elements because the envelope is mostly optically thin by day 200.

We have developed a methodology for using late-time NIR spectra of SNe Ia to determine the initial central density and strength of embedded magnetic field of the WD. Time-series observations in the nebular phase are of great importance because they shed light on the interior structure of the burning products in the SN. There is currently a scarcity of observations showing late-time NIR results for SNe Ia and time evolution observations of the nebular spectra of SNe Ia.

The [Fe II] emission line at 1.644 μm is relatively "clean" compared to most of the NIR region, as was shown in Sections 3 and 5.2, especially when compared with the optical spectra of nebular SNe Ia. The neighboring features to the 1.644 μm line are blended features, with multiple iron and cobalt emission lines contributing, and are therefore not as well-suited to analyze the evolution of line profiles, which has been presented in this work. The [Fe II] 1.644 μm emission line is ideal because of the relatively little line contamination from nearby features.

An early nebular epoch, somewhere around 100 – 200 days past explosion, is needed to pin down the central density of the WD before the magnetic fields in the ejecta start affecting the line width curves. As demonstrated by the models, the line widths of the [Fe II] 1.644 μm line converge when gamma emission still dominates in the nebular phase and is independent of the magnetic field strength embedded in the ejecta. Multiple epochs in the nebular phase are needed in order to probe the evolution of the [Fe II] 1.644 μm emission line and set a lower limit on the magnetic field strength, which plays a role once positron emission dominates.

Finally, we have discussed some implications of a low mass WD and put our results into context of progenitor systems and explosion scenarios. The M_{WD}(SN 2005df) we have obtained is close to M_{Ch}, making a violent or dynamical merger scenario unlikely because those can trigger explosions in a wide range of masses. Within the scenario of M_{Ch} explosions, the thermonuclear runaway is triggered by compressional heating due to accretion of H, He or C as discussed in the introduction. A low central density, such as we found for SN 2005df, requires high accretion rates in M_{Ch} scenarios. For our models, H-accretion would barely be consistent with ignition at our measured ρ_c for SN 2005df, even without Urca process cooling (Barkat & Wheeler 1990; Stein & Wheeler 2006). Our results for SN 2005df may favor He-accretion from a giant companion star in a SD system or C-accretion from a disrupted WD companion in a DD system. Alternatively, SN 2005df may show some central mixing and originate from a WD even closer to M_{Ch}. Note that MIR spectra, with their unblended Ni lines during the first few months when the envelope changes from the optically thick to transparent continua, allow for investigation of possible mixing and M_{Ch} mass explosions (Telesco et al. 2014).

The methods we have developed for line width determination of central density and magnetic fields is applicable to a large range of SNe Ia. Specifically, SN 2014J has very similar light curve characteristics to SN 2005df, with $M_B = -19.19(\pm 0.10)$ and $\Delta m_{15}(B) = 1.12$ (Marion et al. 2014), mid-IR spectra (Gerardy et al. 2007; Telesco et al. 2014), and ^{56}Ni mass based on gamma-ray observations (Churazov et al. 2014; Diehl et al. 2014; Isern et al. 2014). These two SNe appear to be identical in the exterior regions of the explosion but what about the interior regions? NIR spectra should be of high enough signal-to-noise to determine initial WD central density and magnetic fields. Differential comparison of SN 2005df and SN 2014J should therefore put new constraints on the progenitor system and the explosion scenario.

With the observations of SN 2005df presented in this work, we are able to probe central density of the WD but are just on the edge of being able to probe the influence magnetic fields have on the spectra. Moreover, we need a statistical sample to examine the diversity of SN Ia and the variety of explosion scenarios that all may be realized

in nature. With forthcoming instruments like the James Webb Space Telescope, the Very Large Telescope, the Wide-Field Infrared Survey Telescope, the Giant Magellan Telescope, and the Extremely Large Telescope, many more observations of SNe Ia in the nebular phase will be available at better signal-to-noise. Additionally, the available atomic data needed for modeling is increasing and improving. This type of analysis is crucial to understanding the progenitor systems and explosion scenarios, thereby increasing our ability to standardize and use SNe Ia.

ACKNOWLEDGMENTS

We would like to thank many colleagues and collaborators for their support. In particular, many thanks to Eric Hsiao, Mark Phillips, Nidia Morrell, and the Carnegie Supernova Project (CSP) collaboration for invaluable discussion and leading us to the light curve results of Milne et al. (2010) and Brown et al. (2010). The CSP collaboration has provided invaluable opportunities for observational experience and insight into photometry and spectroscopy of SNe Ia in general. This research is based on observations using Gemini South. We would also like to thank the speakers at the Gemini Data Workshop 2010, in Tucson, AZ. The work presented in this paper has been supported in part by NSF awards AST-0708855 and AST-1008962 (PI: Peter Hoeflich) and AST-1009464 (PI: Chris Gerardy). We would also like to express our thanks to Peter van Hoof for creation of *The Atomic Line List* (V2.05B18) at `http://www.pa.uky.edu/ peter/newpage/` and the NIST ADS Team for creation of *The NIST Atomic Spectra Database* (V5.2) at `http://physics.nist.gov/asd`.
Gemini:Gillett(GNIRS)

REFERENCES

Barkat Z. & Wheeler J. C. 1990, ApJ, 355, 602
Benz, W., Cameron, A. G. W., Press, W. H., and Bowers, R. L. 1990, ApJ, 348, 647
Brachwitz, F., Dean, D. J., Hix, W. R., et al. 2000, ApJ, 536, 934
Branch, D., Livio, M., Yungelson, L. R., Boffi, F. R., & Baron, E. 1995, PASP, 107, 1019
Brown, P. J., Roming, P. W. A., Milne, P., et al. 2010, ApJ, 721, 1608
Churazov, E., Sunyaev, R., Isern, J., et al. 2014, Nature, 512, 406
Colella, P., & Woodward, P. R. 1984, J. Chem. Phys., 54, 174
Cyburt, R. H., Amthor, A. M., Ferguson, R., et al. 2010, ApJS, 189, 240
De, S., Baron, E., & Hauschildt, P. H. 2010, MNRAS, 401, 2081
Dessart, L., Blondin, S., Hillier, D. J., & Khokhlov, A. 2014, MNRAS, 441, 532
Diehl, R., Siegert, T., Hillebrandt, W., et al. 2014, arXiv:1409.5477
Di Stefano, R. & Kilic, M. 2012, ApJ, 759, 56
Di Stefano, R., Voss, R., & Claeys, J. S. W. 2011, in AAS/High Energy Division Conf. Ser. 12, Single- and Double-degenerate Models of Type Ia SNe, Nuclear-burning White Dwarfs, Spin, and Supersoft X-ray Sources, 33.04
Edwards, Z. I., Pagnotta, A., & Schaefer, B. E. 2012, ApJ, 747, L19
Evans, R., & Gilmore, A. 2005, Central Bureau for Electronic Telegrams, 192, 1
Evans, R., & Gilmore, A. 2005, International Astronomical Union Circular, 8580, 2
Foley, R. J., McCully, C., Jha, S. W., et al. 2014, ApJ, 792, 29
Friesen, B., Baron, E., Parrent, J. T., et al. 2014, in preparation
Gamezo, V. N., Khokhlov, A. M., & Oran, E. S. 2004, Phys. Rev. Lett., 92, 211102
Gerardy, C. L., Meikle, W. P. S., Kotak, R., et al. 2007, ApJ, 661, 995
González Hernández, J. I., Ruiz-Lapuente, P., Filippenko, A. V., et al. 2009, ApJ, 691, 1
Greiner, J., Hasinger, G., & Kahabka, P. 1991, A&A, 246, L17
Hernanz, M., Isern, J., Canal, R., Labay, J., & Mochkovitch, R. 1988, ApJ, 324, 331
Hoeflich, P. 1990, PhD thesis, Ludwig-Maximilians-Universität, Munich
Hoeflich, P. 2002, arXiv:astro-ph/0207103
Hoeflich, P., & Khokhlov, A. 1996, ApJ, 457, 500
Hoeflich, P., Mueller, E., & Khokhlov, A. 1993, A&A, 268,570
Hoeflich, P. 1995, ApJ, 443, 89
Hoeflich, P. 2006, Nucl. Phys. A, 777, 579
Hoeflich, P. 2009, in AIP Conf. Ser. 1171, Multi-dimensional Radiation Transport in Rapidly Expanding Envelopes, ed. I. Hubeny, J. M. Stone, K. MacGregor, & K. Werner, 161
Hoeflich, P., Gerardy, C. L., Fesen, R. A., & Sakai, S. 2002, ApJ, 568, 791
Hoeflich, P., Gerardy, C. L., Nomoto, K., et al. 2004, ApJ, 617, 1258
Hoeflich, P., Krisciunas, K., Khokhlov, A. M., et al. 2010, ApJ, 710, 444
Hoeflich, P., Dragulin, P., Mitchell, J., et al. 2013, Frontiers of Physics, 8, 2, 144
Howell, D. A., Sullivan, M., Nugent P. E., et al. 2006, Nature, 443, 308
Hoyle, F. & Fowler, W. A. 1960, ApJ, 132, 565
Iben Jr., I., & Tutukov, A. V. 1984, ApJS, 54, 335
Isern, J., Knoedlseder, J., Jean, P., et al. 2014, The Astronomer's Telegram, 6099, 1
Kahabka, P., & van den Heuvel, E. P. J. 1997, 35, 69
Kerzendorf, W. E., Schmidt, B. P., Asplund, M., et al. 2009, ApJ, 701, 1665
Khokhlov, A. M. 1991, A&A, 245, L25
Kramida, A., Ralchenko, Y., Reader, J., & NIST ASD Team. 2014, NIST Atomic Spectra Database (ver. 5.2), [Online]. Available: `http://physics.nist.gov/asd`
Kurucz, R. 1994, Atomic Data for Ca, Sc, Ti, V, and Cr, [CD-ROM No. 20]
Kurucz, R. L. 1993, Atomic data for opacity calculations, [CD-Rom No. 1]
Lorén-Aguilar, P., Isern, J., & García-Berro, E. 2009, A&A, 500, 1193
Maeda, K., Taubenberger, S., Sollerman, J., et al. 2010, ApJ, 708, 1703
Marion, G. H., Hoeflich, P., Wheeler, et al. 2006, ApJ, 645, 1392
Marion, G. H., Hoeflich, P., Gerardy, C. L., et al. 2009, AJ, 138, 727
Marion, G. H., Sand, D. J., Hsiao, E. Y., et al. 2014, arXiv:1405.3970
Maund, J. R., Hoeflich, P., Patat, F., et al. 2010, ApJ, 725, L167
McCully, C., Jha, S. W., Foley, R. J., et al. 2014, Nature, 512, 54
Mihalas, D., & Mihalas, B. W. 1999, Foundations of Radiation Hydrodynamics
Milne, P. A., Brown, P. J., Roming, P. W. A., et al. 2010, ApJ, 721, 1627
Motohara, K., Maeda, K., Gerardy, C. L., et al. 2006, ApJ, 652, L101
Nomoto, K., Thielemann, F.-K., & Yokoi, K. 1984, ApJ, 286, 644
Nomoto, K., Uenishi, T., Kobayashi, C., et al. 2003, From Twilight to Highlight: The Physics of Supernovae
Ochsenbein, F., Bauer, P., & Marcout, J. 2000, A&AS, 143, 23
Paczyńsky, B. 1972, Astrophys. Lett., 11,53
Pakmor, R., Kromer, M., Taubenberger, S., Sim, S. A., Röpke, F. K., & Hillebrandt, W. 2012, ApJ, 747, L10
Patat, F., Hoeflich, P., Baade, D., et al. 2012, A&A, 545, A7
Penney, R. & Hoeflich, P. 2014, ApJ, 795, 84
Penney, R. B. 2011, PhD thesis, Florida State University
Phillips, M. M. 1993, ApJ, 413, L105
Piersanti, L., Gagliardi, S., Iben, Jr., I., & Tornambé, A. 2003, ApJ, 583, 885
Piersanti, L., Tornambé, A., Straniero, O., & Domìnguez, I. 2009, in AIP Conf. Ser. 1111, The Progenitors of Thermonuclear Supernovae, ed. Giobbi, G., Tornambé, A., Raimondo, G., Limongi, M., Antonelli, L. A., Menci, N., & Brocato, E., 259

Quimby, R. M., Hoeflich, P., Wheeler, J. C., et!al. 2007, ApJ, 666, 1083
Quinet, P. 1996, A&AS, 116, 573
Quinet, P. 1998, A&AS, 129, 147
Quinet, P., Le Dourneuf, M., & Zeippen, C. J. 1996, A&AS, 120, 361
Rappaport, S., Chiang, E., Kallman, T., & Malina, R. 1994, ApJ, 431, 237
Röpke, F. K., & Niemeyer, J. C. 2007, A&A, 464, 683
Rubin, D., Knop, R. A., Rykoff, E., et al. 2013, ApJ, 763, 35
Ruiz-Lapuente, P., Comeron, F., Méndez, J., et al. 2004, Nature, 431, 1069
Sadler, B. 2012, PhD thesis, Florida State University
Saio, H., & Nomoto, K. 1985, A&A, 150, L21
Saio, H., & Nomoto, K. 1998, ApJ, 500, 388
Schaefer, B. E., & Pagnotta, A. 2012, Nature, 481, 164
Seaton, M. J. 2005, MNRAS, 362, L1
Seitenzahl, I. R., Ciaraldi-Schoolmann, F., & Röpke, F. K. 2011, MNRAS, 414, 2709
Shen, K. J., Bildsten, L., Kasen, D., & Quataert, E. 2012, ApJ, 748, 35
Sim, S. A., Seitenzahl, I. R., Kromer, M., et al. 2013, MNRAS, 436, 333
Stein, J., & Wheeler, J. C. 2006, ApJ, 643, 1190
Stein, J., Barkat, Z., & Wheeler, J. C. 1999, ApJ, 523, 381
Stone, J. M., Mihalas, D., & Norman, M. L. 1992, ApJS, 80, 819
Sugimoto, D., & Nomoto, K. 1975, PASJ, 27, 197
Telesco, C. M., Hoeflich, P., Li, D., et al. 2014, ApJ, submitted
Thielemann, F.-K., Nomoto, K., &Yokoi, K. 1986, A&A, 158, 17
Tornambé, A., & Piersanti, L. 2013, MNRAS, 431, 1812
van den Heuvel, E. P. J., Bhattacharya, D., Nomoto, D., & Rappaport, S. A. 1992, A&A, 262, 97
van Hoof, P. 2014, The Atomic Line List (ver. 2.05B18), [Online]. Available: `http://www.pa.uky.edu/~peter/newpage/`
Wang, B., & Han, Z. 2012, New A Rev., 56, 122
Webbink, R. F. 1984, ApJ, 277, 355
Whelan, J., & Iben, Jr., I. 1973, ApJ, 186, 1007
Woosley, S. E., & Weaver, T. A. 1994, ApJ, 423, 371
Yamaoka, H., Nomoto, K., Shigeyama, T., & Thielemann, F. K. 1992, ApJ, 393, L55